ORIGINAL RESEARCH ARTICLE

Effect of Heat Input on Microstructure and Mechanical Properties of Automated Tungsten Inert Gas-Welded Dissimilar AA6061-T6 and AA7075-T6 Joints

Md Saquib Bin Reyaz ⓘ and Amar Nath Sinha

This study explored the heat input effects on automated TIG welded dissimilar AA6061-T6 and AA7075-T6 joints using filler ER5356. Three heat input welded samples, namely HI1 (0.73 kJ/mm), HI2 (1.69 kJ/mm), and HI3 (2.27 kJ/mm), were utilized and their corresponding microstructure and grain boundary features were investigated and correlated with the joint's mechanical properties. Electron backscattered diffraction (EBSD) results showed that the low-angle grain boundaries (LAGBs) in the base alloys transformed into high-angle grain boundaries (HAGBs) in the fusion zone (FZ) after welding. However, the grain boundary transformations were more pronounced in the high heat input welded sample HI3. Pole figures revealed strong dominance of A_1^*/A_2^* and A/ $-A$ textures with a small amount of C and B/ $-B$ textures at the FZ for all the heat input joints. Orientation distribution functions also exhibited the recrystallization textures P {011} $<112>$ and Goss {110} $<001>$, plane strain texture S {123} $<634>$ with some deformation texture H {001} $<110>$ at the FZ center. The medium heat input sample HI2 had the highest tensile strength of 182 MPa, elongation of 14.4%, and flexural strength of 202 MPa; while, the welded sample HI1 had the highest microhardness of 81 HV when compared to other welded samples. The HI2 joint fracture surface exhibits fine dimples devoid of porosities, suggesting ductile fracture manner. However, the fracture surface of the HI3 joint displayed both smooth and rough cleavage facets with coarser dimples, resulting in a combination of ductile and brittle fracture modes.

1. Introduction

Aluminum and its alloys are remarkable lightweight materials used in a variety of applications such as structures, automotive and maritime parts, and aerospace components due to their great formability, outstanding corrosion resistance, and significant strength (Ref 1-3). AA6061-T6 finds application in storage tankers, naval sections, pipes, and high-speed trains, and various other industries; while, AA7075-T6 is predominantly employed in the fields of aerospace components including airplane wings, panels, and aircraft fuselage (Ref 4-6). The chief alloying elements in AA6061-T6 alloy are Mg and Si, while Mg, Zn, and Cu are the main alloying elements in AA7075-T6 alloy; these alloying elements strengthened these alloys through precipitation hardening (Ref 7-9). Riveting is a classic technique for joining AA6061-T6 and AA7075-T6, although it causes stress concentration and increases joint weight, limiting its use in aircraft (Ref 10, 11). Welding is a common and vital method for making high-quality joints to overcome these restrictions (Ref 12).

Tungsten inert gas (TIG) welding is often the most recommended fusion welding process for fabricating aluminum and its alloys because it is simple, adaptable, applicable, and cost-effective (Ref 13-15). Despite the fact that solid-state welding methods like friction stir welding (FSW) produce high-quality, defect-free welds, their implementation has certain drawbacks, including the need for adequate fixtures, clamping mechanisms, and trained operators, all of which drive up the cost of the welding process. In addition, FSW is restricted to producing solely horizontal joints and is not suitable for welding joints with complex shapes (Ref 16-22). However, researchers struggle to join dissimilar tungsten inert gas (DS-TIG) joints of Al alloys (Ref 15, 23). Oxygen and aluminum chemically interact to create a resilient layer of aluminum oxides, while increased hydrogen dissolvability creates voids (Ref 24). Moreover, different chemical and thermal characteristics of aluminum alloys cause solidification fractures, post-weld residual strains, and thermally affected region softening (Ref 24-26).

To ensure effective and quality joints in aluminum and its alloys, one can utilize low heat input methods like FSW (Ref 27-30) or adjust welding parameters to regulate heat input during arc welding (Ref 31). Researchers have extensively studied the heat input in fusion welding, which refers to the energy supplied by the arc source per unit length of the weld. Rojas et al. (Ref 32) published a study on the impact of heat input on the fatigue properties and microstructure of AA6061 butt joints during TIG welding. They deduced that low heat

Md Saquib Bin Reyaz and Amar Nath Sinha, Department of Mechanical Engineering, National Institute of Technology Patna, Bihar 800005, India. Contact e-mail: mdr.phd19.me@nitp.ac.in.

input resulted in degraded tensile properties due to partial penetration and significant voids. Samiuddin et al. (Ref 33) studied the impact of various heat inputs on the microstructure as well as the mechanical characteristics of TIG welded AA5083 aluminum joints that involve tensile strength, Charpy impact toughness, and microhardness. The findings confirmed that the medium heat input (1-2 kJ/mm) yielded optimal mechanical features by eliminating weld imperfections, resulting in a loss of only approximately 18.26% of strength. Cevik (Ref 34) studied the impact of various currents on the microstructure and mechanical properties of TIG welded AA7075-T651 joints. As the weld current increased, they found that the heat inputs also increased. This led to a coarser grain and the formation of micro-thermal cracks, which in turn caused a decrease in impact and hardness strengths of the joint. Reyaz and Sinha (Ref 35) adjusted heat input and improved mechanical and wear properties of DS-TIG joints of AA6061-T6 and AA7075-T6 alloys by varying current, weld speed, and arc voltage. The medium heat input joint with 145 A current, 78 mm/min weld speed, and 1.67 kJ/mm heat input had the maximum tensile strength, ductility, impact toughness, and wear resistance of the joint. They proposed that regulated heat input may build finer structures and consistent intermetallic dispersion without voids. Heat input affected mechanical characteristics and corrosion rates of cold metal transfer (CMT)-welded AA5754 and AA6061 alloys, according to Comez and Durmus (Ref 36). High heat input induced partially melted region expansion and grain coarsening in AA5754 and overaging in AA6061, reducing joint tensile strength. The lowest heat input welded junction has the lowest corrosion rate.

Yuruk et al. (Ref 22) examined the impact of current intensity and weld speed on the mechanical features of dissimilar AA5754/AA6013 alloys in metal inert gas (MIG) joints. The highest mechanical properties, such as hardness, bending strength, and fatigue resistance, were observed at a weld current of 150 A, a weld speed of 150 mm/min, and a heat input of 96 J/mm. They proposed that when the weld current rises, the grain structures in the fusion region become coarser due to enhanced heat input, leading to a decline in joint properties. Ma et al. (Ref 37) investigated the influence of different intermetallic compounds on the mechanical and wear performance of fusion welded joints of aluminum/steel joint at different heat inputs. The results show that a low heat input should be utilized to obtain the good joint's corrosion resistance and mechanical performance. Ye et al. (Ref 38) evaluated the microstructure and mechanical properties of TIG-MIG hybrid welded aluminum/steel joint. They found excellent weld bead appearance, controlled intermetallic compounds and the tensile strength of 148.1Mpa resulted in lower heat input compared to traditional MIG joint.

Qin et al. (Ref 39) studied the impact of two welding currents (125 and 135 A) and a constant weld speed (10 mm/s) on the microstructural changes and mechanical properties of TIG welded $Al - Mg_2Si$ joints. Electron backscattered diffraction results showed that the low-angle grain boundaries (LAGBs) in the base metal changed to high-angle grain boundaries (HAGBs) following welding. The base metal had three preferred orientations with a maximum orientation density value of 26.31. However, the quality of the welded joints decreased, with a maximum orientation density of only 2.75. The joints welded at 125 A had less tensile strength and ductility than the joints welded at 135 A. Guo et al. (Ref 40) examined residual stress distributions and texture development

in FSW in different AA2024-T3 and AA7075-T6 welded joints. They observed that AA7075-T6 had a larger longitudinal residual stress than AA2024-T3. AA7075 had tensile transverse and normal residual stresses, whereas AA2024 had compressive ones. KAM maps of the thermomechanically impacted zone showed more local plastic deformation than the weld region, explaining the longitudinal residual stress double peak structure. Wang et al. (Ref 41) used FSW to make distinct AA5052 and AA6061 joints and studied their microstructural and texture evolutions. It was found that the base metal's {001} <100> Cube and {123} <634> S components gradually change to {111} <112> shear texture under shear stress. HAGBs were prevalent in the stir region, then on the retreating side, and finally on the advancing side.

The literature reviewed (Ref 22, 32-38) reveals that the previous studies mainly focused on the impact of heat input on the microstructure and mechanical features of weldments of aluminum and its alloys. However, very limited literature (Ref 39-41) related to the impact of heat inputs on grain boundary variations during TIG-welding of AA6061-T6 and AA7075-T6 alloys was found. Grain boundary studies provided detailed insights into the effects of heat input during TIG welding on deformation and recrystallization behavior. Therefore, the present study investigated the microstructural and grain boundary variations due to the application of different heat inputs and correlate them with their mechanical characteristics, including the tensile, flexural, and microhardness strengths of DS-TIG AA6061-T6 and AA7075-T6 joints. Microstructural features were determined through optical microscopy, scanning electron microscopy (SEM), energy diffraction scanning (EDS), and X-ray diffraction (XRD) techniques; while, grain boundary variations were studied through electron backscattered diffraction (EBSD) technique. Using EBSD, the inverse pole figure (IPF) map, average grain size (AGS), grain boundary misorientation angles (MAs) distribution, pole figures (PFs), and orientation distribution functions (ODFs) in the fusion region were investigated. Profound tensile fractographic examinations were also carried out through SEM and spectroscopic analysis to validate the experimental findings.

2. Materials and Experimental Descriptions

Rolled base alloys AA6061-T6 and AA7075-T6 each of dimension $150 \times 50 \times 6$ mm^3 dimension and the filler wire ER5356 (Ref 13, 42) were utilized in this study. T-6 temper in the aviation sector refers to solution treatment for 1 hour at 470 degrees Celsius, water quenching, and artificial aging for 24 hours at 120 degrees Celsius (Ref 43). Table 1 shows the elemental compositions (weight %) of base alloys and filler metal determined by EDS method.

Figure 1 represents the schematic of experimentation process of an automated TIG welding. A robotic TIG setup (KEMPPI MasterTig 335 ACDC G) featuring an air-cooled flame head used to produce dissimilar tungsten inert gas (DS-TIG) joints in butt configuration as illustrated in Fig. 1(a). A butt joint was made on one side, featuring a 1.5 mm root gap between the plates with a groove angle of 90° and dimensions of 150 mm. Both plates were cleaned well before being mounted on a 200 mm × 200 mm mild steel base plate and clamped firmly in place. Clamps and bolts were employed to prevent plates from warping in either direction as a result of

Table 1 Elemental composition (weight %) of base alloys and filler wire obtained by EDS analysis

Material	Cu	Zn	Mg	Mn	Cr	Ti	Fe	Si	Al
AA7075-T6	1.2	5.2	2.2	0.04	0.3	0.01	0.38	0.43	90.24
AA6061-T6	0.16	0.025	0.88	0.09	0.18	0.15	0.28	0.67	97.56
ER5356	0.016	0.02	4.8	0.15	0.12	0.09	0.14	0.03	94.63

welding's heat. The groove in center of the backing plate is machined to be 12 mm broad and 1.5 mm deep. The groove was cut to lessen the chilling effect at the root, enabling improved penetration. Welding parameters and their ranges were decided based on trial experiments and relevant literature (Ref 13-15, 35). Initial trial examines revealed that an arc length of 3 mm, an angle of 90 degrees at the tip, and a flow rate of 18 l/min generated adequate heat without snuffing out the arc. The variable parameters and constant parameters utilized in the fabrication of DS-TIG joints are shown in Table 2 and 3. Wire feed speed and welding rate were precisely regulated utilizing a wire feed unit and a controller equipped with welding setup. When the welding was finished, the welded plates were left out in the open to cool. The heat input produced during each pass of the welding process is expressed as follows (Ref 15):

$$Q_{\text{inp}} = \eta_{\text{th}} \times \frac{U \times I \times 60}{WS} \qquad \text{(Eq 1)}$$

where Q_{inp}, U, I, and WS stand for the amount of heat input (in J/mm), weld current (in A), arc voltage (in V), and weld speed (in mm/min), respectively. The arc efficiency (η_{th}) during the welding operations was taken as 75% (Ref 44-46).

Microstructural samples were sliced from the DS-TIG joints utilizing wire electric discharge machining (WEDM). The welded samples were meticulously ground and polished via abrasive papers (started from 220 grit size and progressed up to 2200 grit size). Next, they were diamond polished with 0.5 μm grit size diamond paste and etched with Keller's reagent for 15 seconds to achieve mirror finish. The well-polished samples were examined through a stereo microscope (Olympus-SC30, India) and the distribution of different elements in the fusion zones (FZs) were examined with SEM (Make: Zeiss SU-PRA40) equipped with an EDS detector. Phase analysis was employed by using XRD machine (Empyrean, Malvern PANalytical diffractometer). The XRD results were collected with λ = 1.5418 Å and 2θ levels of 10-90°, utilizing a CuKα radiation. For EBSD analysis, the exposed surface of the welded samples was first electropolished in an 80:20 mixture of methanol and perchloric acid solution at an applied voltage of 15 V for 20 seconds at a temperature of − 5 °C. A SEM (Make: Quanta 3D FEG) was then used to do EBSD scans of the WMs of several welded samples. These scanned images were recorded at a step size of 0.2 μm and subsequently analyzed on TSL OIM (orientation imaging microscopy) analysis software 8.0.

Tensile and flexural tests (without reinforcement) were conducted to examine the mechanical strength of DS-TIG joints. The sample design representation for different tests, including a close-up view of tensile and flexural samples is shown in Fig. 1(b), (c) and (d). Tensile and flexural tests were conducted on a Zwick/Roell Z250 model universal testing machine at a strain rate of 1 mm/min as per ASTM E8-M04

standard and ASTM E22-04 standards, respectively. Micro-hardness tests were also performed across the mid region of the weld cross section to a mirror-finished surface using a Vickers hardness tester (UHL-002) in accordance with the ASTME384-11 standard. During the microhardness testing, a load of 200 gf was applied for 18 seconds. In order to produce a more precise result, this study reports the average of three separate measurements taken for each heat input scenario.

## 3. Results and Discussions

3.1 Macroscopic Features

Macroscopic assessment is crucial aspect of determining the success of welding, especially when joining DS-TIG aluminum joints. Figure 2 illustrates the top and bottom views of the weld beads, as well as a cross sectional perspective of the macrographs under different heat inputs. Visual inspection reveals no joint problems like thermal cracks, spatter, etc., for all the three heat input joints, as shown in Fig. 2(a), (b) and (c). The existence of uniform ripples, negligible spatter and no significant deformations in the transverse or longitudinal orientations of the fabricated plates were discovered for all the joints ensures that the developed fixture serves the purpose. However, lack of fusion is observed in the bottom part of the bead near the joint line as marked by red area in Fig. 2(a) is due to incomplete mixing of base alloys with filler metal. Whereas excess penetrations are observed on bottom view of the weld bead as seen from Fig. 2(c) is due to increased weld heat input. Furthermore, HI1 joint shows notable porosities; while, HI2 and HI3 joints showed minimum porosities, which indicated that they were correctly welded.

Examination of the weld cap width measurements in Fig. 2 also reveals that reducing weld speed from 98 to 77 mm/min and raising weld current from 100 to 145 A caused a 36.17% increase in bead width. Likewise, elevating weld current from 145 to 165 A and decreasing weld speed from 77 to 72 mm/min led to a 10.15% increase in bead width. The fluctuations in weld bead width likely stemmed from modifying heat input, which occurred when adjusting either the welding speed or the current (Ref 33). Raising the welding speed diminishes the weld pool's dimensions, resulting in a reduction in both the accumulated metal volume and the weld width. This adjustment affects the quantity of metal buildup, heat input, and the rate of weld cooling (Ref 22). Figure 3 depicts the estimated weld width (WW), weld penetration depth (WP), and weld reinforcement (WR) for the various heat input weldments. The findings demonstrate that the WW, WP, and WR fall within the range of 9.4-14.1, 4.1-6.9, and 1.9-2.5 mm, respectively, concerning heat input. The weld's width and penetration depth varied linearly with heat input. An excess WP of 6.9 mm was noticed in a weld sample of HI3 with a high heat input of
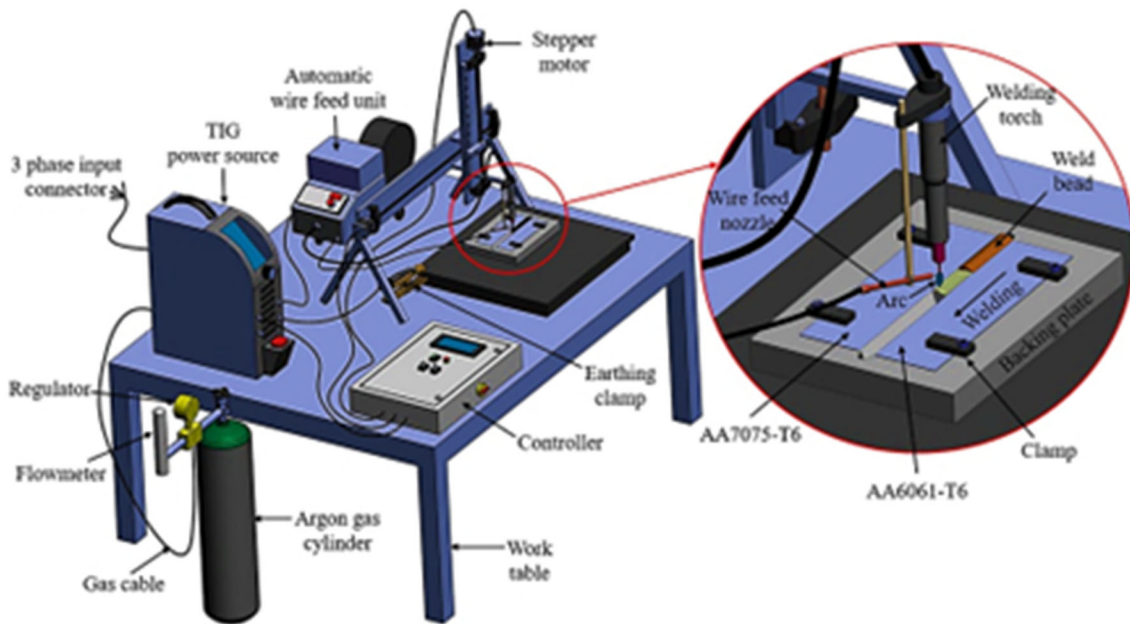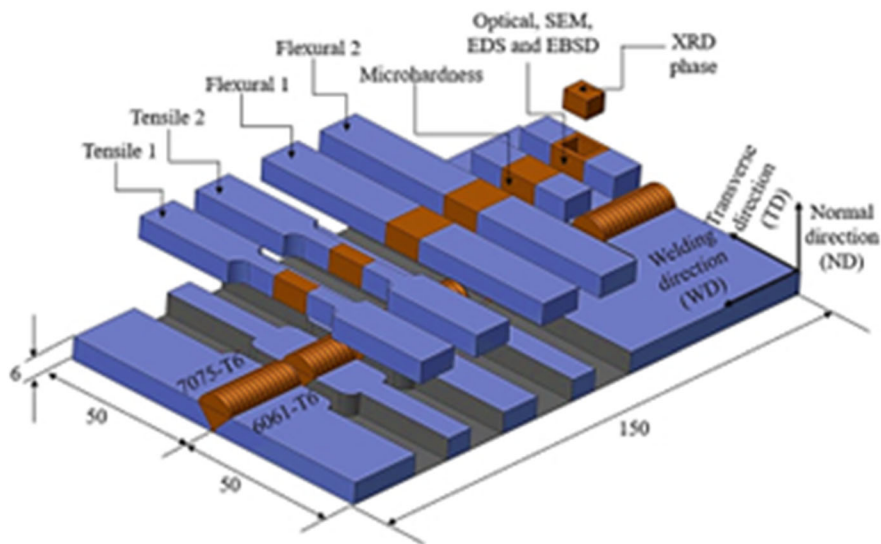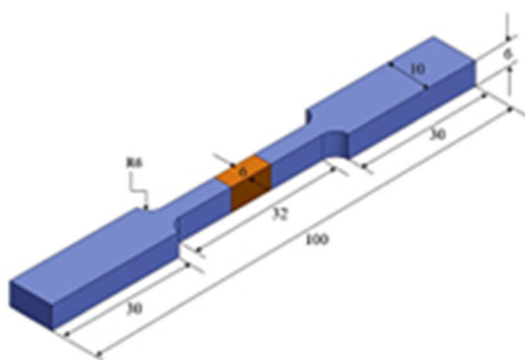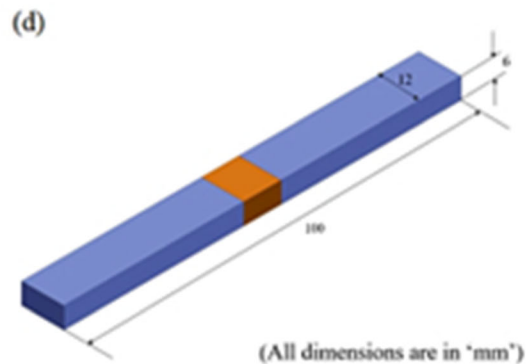
Fig. 1 An illustration of (a) an automated TIG welding system (b) sample design for various characterizations (c) tensile specimen with dimensions and (d) flexural specimen with dimensions

2.27 kJ/mm. Koli et al. (Ref 47) reported a similar observation in their study. They connected a 2 mm thick plate of AA6082-T6 to a 3.18 mm thick plate of AA6061-T6 and found a maximum WP of 3.7 mm for the high heat input CMT welded joint. By elevating the heat input, the welding arc comes into contact with a larger portion of the base and filler metals, which leads to the creation of a more extensive and deeper penetration (Ref 35). The maximum WR was 2.5 mm, and the minimum was 1.9 mm, indicating a decreasing trend. The WR linearly increased with increasing heat input up to approximately 1.69 kJ/mm, and then it dropped dramatically to a final value close to its minimum.

Table 2 Variable DS-TIG welding parameters to acquire different heat inputs

Sample	Weld current, A	Arc voltage, V	Weld speed, mm/min	Wire feed speed, m/min	Heat input, kJ/mm
HI1	100	16	98	1.6	0.73
HI2	145	20	77	2.3	1.69
HI3	165	22	72	3.1	2.27

Table 3 Constant DS-TIG welding parameters

Tungsten electrode diameter, mm	3.2
Filler rod diameter, mm	2.4
Arc length, mm	2.5
Polarity	A.C
Number of passes	2
Torch angle (degree)	90
Shielding gas	Argon (99.99 % pure)
Argon flow rate, l/min	18

3.2 Microstructural Variations

Heterogeneous microstructures evolved as a result of the varied chemical compositions and solidification behaviors of the filler wire and aluminum alloys as they reacted with one another during the melting process, which are responsible for the formation of different zones. Each joint basically consists of mainly four zones: the base metal alloy (BM), the heat affected zone (HAZ), the partially melted zone (PMZ), and the fusion zone (FZ).

Figure 4 shows the optical micrographs and XRD peaks of the base metal alloys (BMs) AA6061-T6 and AA7075-T6, respectively. AA6061-T6 consists of grains with an average diameter of approximately 18.34 μm; whereas, AA7075-T6 exhibits elongated grains oriented along the rolling direction, featuring an average diameter of around 22.16 μm, as illustrated in Fig 4(a) and (b). There are some black inclusion particles were appeared in the interior of the grains and at the grain boundaries (GBs), which are responsible for the intermetallic phase evolutions. XRD results exclusively displaying the presence of the Mg_2Si phase for AA6061-T6 and $MgZn_2$ and Al_2CuMg isomorphous phases for AA7075-T6 alloy
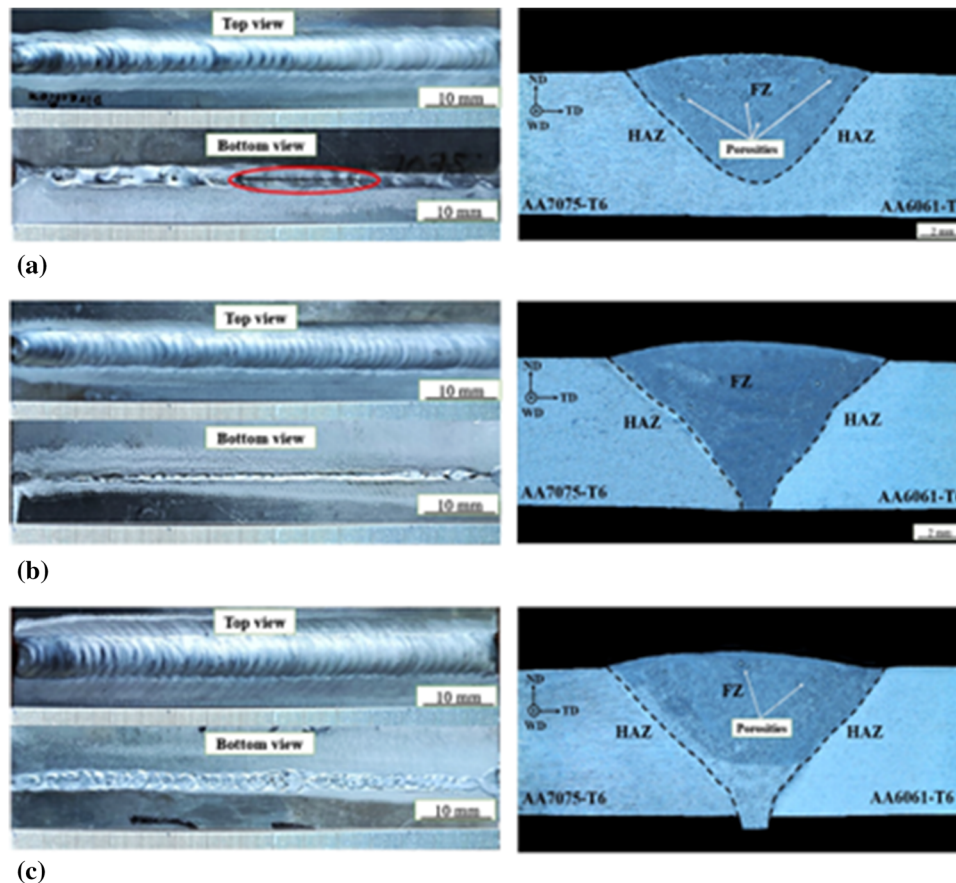
Fig. 2 Weld bead surfaces (top and bottom perspective) and macrographs of DS-TIG joints (a) HI1, (b) HI2 and (c) HI3
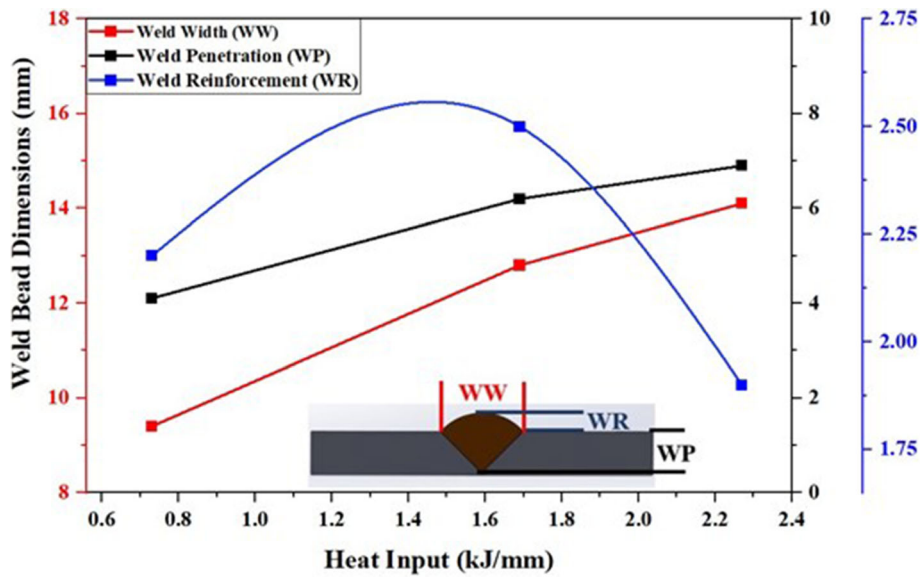
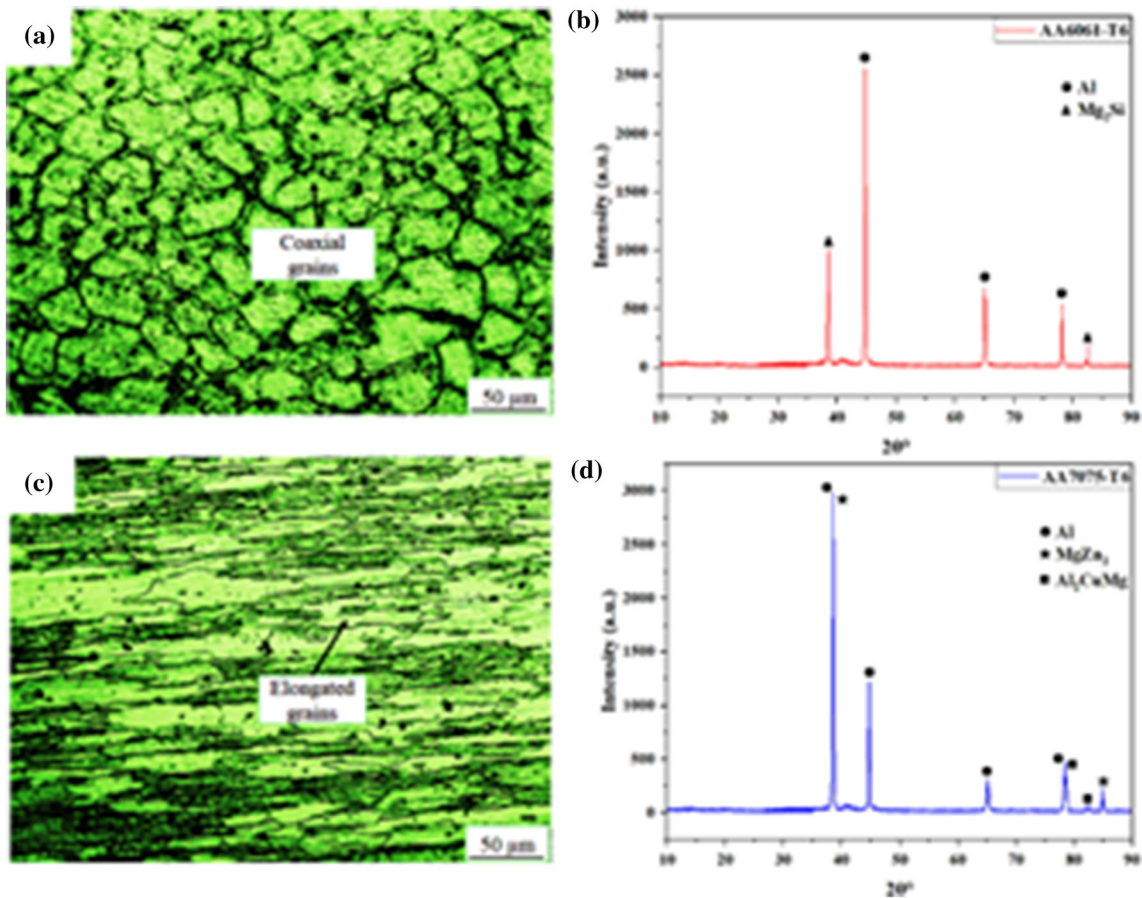**Fig. 3** Weld bead dimensions of DS-TIG joints at different heat inputs

Fig. 4 Optical micrographs and XRD pattern of the base alloys (a, b) AA6061-T6 and (c, d) AA7075-T6

(Fig. 4c and d). It should be noted that Al_2Cu phase is not appeared in the XRD pattern for the base metal AA6061-T6, since the amount of this phase was too small (Ref 39).

Figure 5 displays optical micrographs of the various zones in DS-TIG joints HI1, HI2, and HI3, respectively. The HAZ endured higher temperatures, but not hot enough to melt,

causing structural changes due to the welding thermal cycles (Ref 9). Figure 5(a), (b) and (c) shows larger, elongated grain in the AA7075 HAZ, which are similar to the grains observed in base alloy AA7075 (Fig. 4c), likely due to the lamination impact (Ref 24). However, the microstructure in AA7075 HAZ is mainly influenced by two distinct types of solid-state
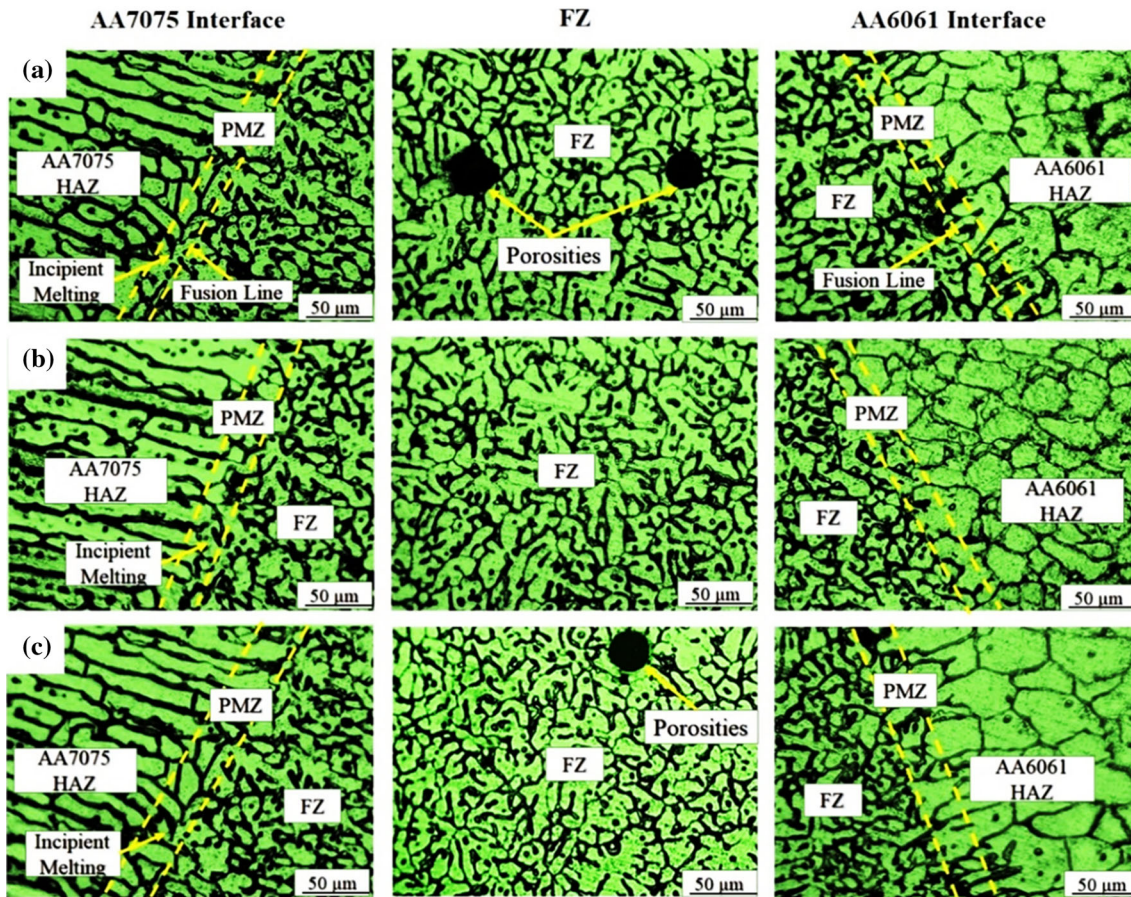
Fig. 5 Optical micrographs of various zones of DS-TIG joints: (a) HI1, (b) HI2, and (c) HI3

reactions (Ref 8, 15). The microstructure in AA6061 HAZ exhibited grains similar to the base metal AA6061-T6 with eutectic Mg_2Si phase (Ref 48), as displayed in Fig. 4(a). However, the eutectic Mg_2Si phase differs from the base metal AA6061-T6 and undergoes a reduction, with some parts transforming into a dot-like structure. The PMZ is a solid–liquid interface zone close to the fusion line that contains a directional columnar structure in the vicinity of the FZ along the direction of heat dispersion (Ref 49). The PMZ area on both sides of the fusion line is raised with the heat input, as is evident in Fig. 5(a), (b), and (c). The area of the PMZ near the AA6061 side is lesser compared to AA7075 side. The increased thermal conductivity of AA6061-T6 results in a faster solidification (Ref 50), thereby limiting particle growth and generating a smaller surface area. Moreover, in the AA7075 PMZ, typically columnar grains and incipient melting at GBs were observed due to the broad freezing range of the AA7075-T6 (Ref 8).

Figure 5(a), (b) and (c) displays the non-equilibrium as-cast structure of equiaxed grain formations in the FZ, which is induced through proper undercooling and diverse nucleation during high thermal cycles (Ref 49). Due to the high temperatures in the fusion zone (FZ), the grains endure significant recrystallization. Yet, during fusion welding, rapid cooling causes nucleation in multiple grains, resulting in the formation of equiaxed grains. Figure 6(a), (b) and (c) displays SEM images of the HI1, HI2, and HI3 joints in the FZ center. The corresponding void size distribution is represented in Fig. 6(d), (e) and (f). A zoomed SEM image of the labeled

square region (Fig. 6g) provides a clear and detailed description of the characteristics of FZ in HI2 joint, which reveals the presence of equiaxed grains and more uniform dispersion of intermetallic phases. Additionally, spot EDS analysis (Fig. 6h) conducted on the white particles shows the presence of significant Cu, Zn and Mg, which confirms the existence of intermetallic phases such as $MgZn_2$ and Al_2CuMg were formed within the FZ during the welding process. Similar intermetallic phases were reported by other studies in welding of dissimilar 6061-T6 and 7075-T6 aluminum alloys (Ref 15, 51). The grain segregation behavior also occurred in the FZ of the HI2 joint, as shown in Fig. 6(g). During welding, the increased heat input led to the creation of a larger molten basin, which explains the observed phenomenon. Consequently, a significant amount of the filler wire was melted and incorporated into the pool, resulting in an increased fusion ratio of the weld bead (Ref 39).

Porosity is a kind of void that was generally formed in the DS-TIG joints, as indicated by the white arrows in Fig. 6(a), (b) and (c). In the case of HI1 welding, the shielding gas effectively guards the top surface but does not provide protection for the molten pool's rear surface, permitting ambient air to infiltrate the molten pool (Ref 15). However, HI2 and HI3 joints exhibited very low porosities in the FZ, as the increased heat input reduces the chance of porosity formation (Ref 15). In a study, Peng et al. (Ref 48) joined AA6061-T6 TIG joints and deduced that low heat input resulted in partial penetration with significant voids. The diameter of porosity, referred to as the equivalent circle diameter (ECD) of voids, was measured using ImageJ software. To illustrate the void size distribution for
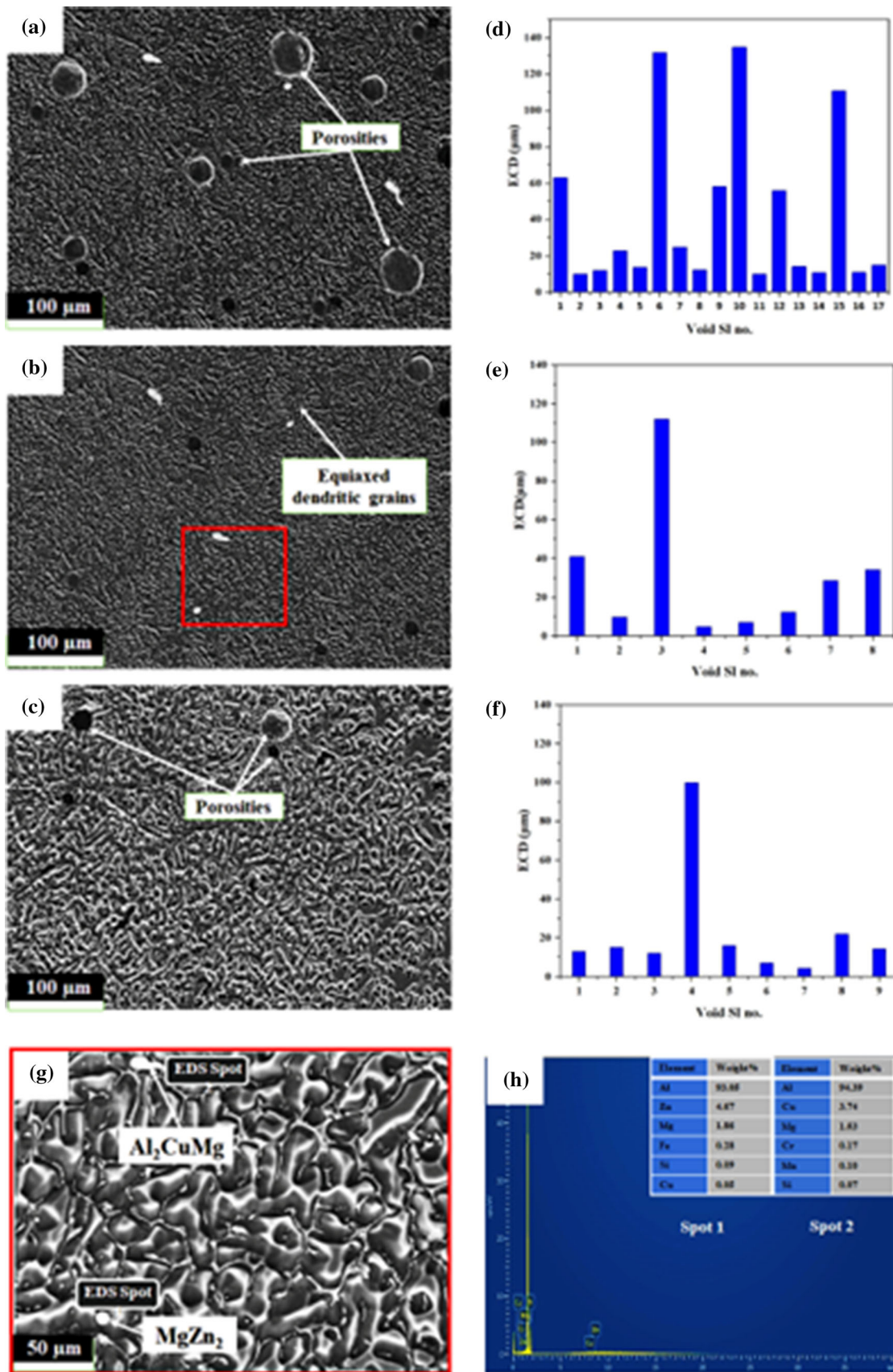
Fig. 6 SEM images at the FZ center of DS-TIG joints: (a) HI1, (b) HI2 and (c) HI3; Bar graph displays the corresponding void size distributions in the FZ (d) HI1, (e) HI2 and (f) HI3; (g) Magnified view of square region marked in (b); (h) EDS analysis of different spots marked in (g)
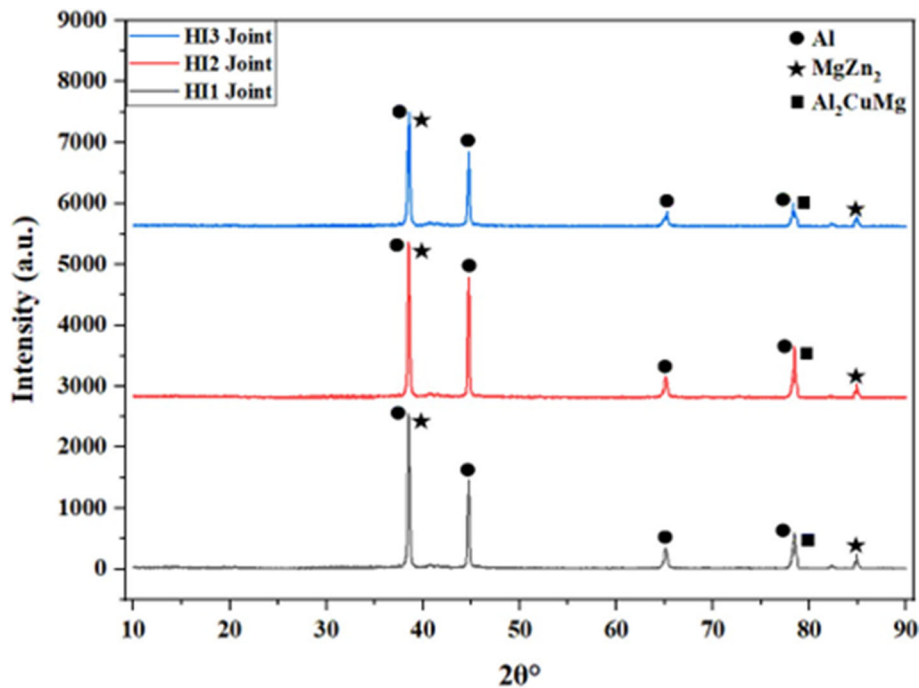
Fig. 7 XRD peaks of DS-TIG joints at various heat inputs

joints exposed to different heat inputs, the bar graph was drawn for samples HI1, HI2, and HI3 and displayed in Fig. 6(d), (e) and (f). The ECD for HI1, HI2, and HI3 were calculated approx. 576, 165 and 209 μm, respectively. This suggests that HI2 welded joint was properly fused as compared to the other welded joints with minimum porosities formation. It is evident that as the weld current increases or the weld speed decreases, the resulting heat input to the weld increases which further decreases the ECD of voids; however, high heat input raised the ECD of voids to some extent (Ref 26).

Figure 7 displays the XRD peaks of DS-TIG joints at various heat inputs to see the phase variations within the FZ. Similar to the base alloy AA7075-T6 (Fig. 5d), the FZ still contained of $MgZn_2$ and Al_2CuMg phases along with aluminum (Al). As seen in Fig. 4(b), (d), and (7), the peak intensity ratio between the $MgZn_2$ phase and the Al phase decreased significantly, indicating a shift in phase content between the BMs and FZ. Also, the Al_2CuMg concentration was much lower in the FZ compared to the BM. The greatest intensity in the FZ fluctuates with heat inputs. Due to grain size, texture, and dynamic grain migration and sub-grain boundaries during welding, this diversity occurs (Ref 52). There was a marginal change in peak intensities for HI1 joint with respect to HI2 joint; while, HI3 joint exhibited significant decrease in peak intensities with respect to HI1 joint in the FZ (Fig. 7). The HI3 joint had lower peak intensities, showing that high heat inputs vaporized Mg from the molten weld pool at high temperatures (Ref 47), and residual Mg interacted with Zn and Cu to generate the reduced $MgZn_2$ and Al_2CuMg phases. Liu et al.(Ref 53) observed the similar phenomena that the Zn and Mg elements were partially vaporized in FZ during the TIG welding of AA7075 alloys. It may be inferred that weld heat input strongly influences the microstructural characteristics, including grain structures, intermetallic phase variations, and porosity formations, which may further affect the mechanical

properties (tensile, flexural, and hardness strengths) of the welded joints.

3.3 Grain Boundary Features

Figure 8 represents the EBSD micrographs showing IPF map with color-coded scale, grain size (GS) distribution, and grain boundary MAs distribution across the FZ center for different heat input samples. The IPF map displays the transverse direction (TD), weld direction (WD), and normal to weld direction (ND) with respect to the crystal's $<110>$, $<111>$, and $<001>$ orientations. The different colors in IPF maps represent crystallographic orientations of the various grains. The average grain size (AGS) in the case of HI1 and HI2 joints are 25.42 ± 8.83 and 29.85 ± 13.68 μm, respectively (Fig. 8b and e); while, AGS is 44.63 ± 15.18 μm for the HI3 joint. It can be noted that the low and medium heat input samples exhibited relatively fine grain structures compared to high heat input sample (Fig. 8h). This was due to the fact that low and medium heat input joints resulted in a rapid cooling rate of the weld pool due to a smaller weld pool size. This quick solidification promotes a higher degree of supercooling, facilitates the grains nucleation and restricts the grain growth, leading to the formation of a fine-grained FZ structures (Ref 15). Also, it was found in the literature that recrystallization is the main cause of the formation of new grains in the FZ during fusion welding of aluminum alloys (Ref 39, 54). In the recrystallization process, the low-angle grain boundaries (LAGBs) of the base metals keep moving and changing into high-angle grain boundaries (HAGBs) in the FZ (Ref 55, 56). This happens because sub-grains join together, making new recrystallized grains (Ref 57).

The color-coded orientation maps (Fig. 8c, f and i) showed both LAGBs with an average misorientation of 2°-15° and HAGBs with a misorientation of more than 15°. Figure 9 represents the statistics of percentage of LAGBs, AGS, and
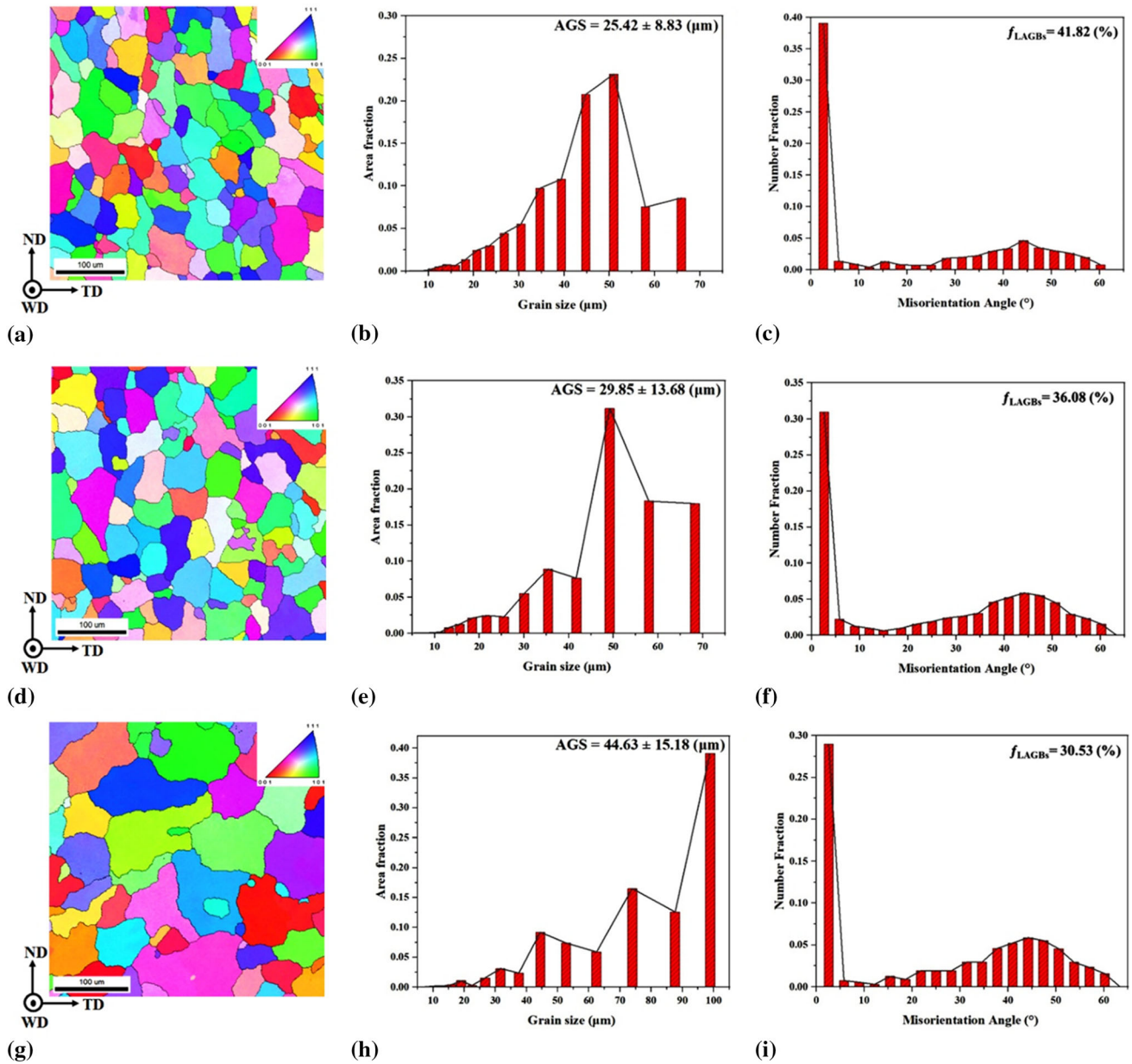
Fig. 8 EBSD micrographs showing IPF map (with color-coded scale), GS distribution and grain boundary MAs distribution across the FZ center of DS-TIG joints (a-c) HI1, (d-f) HI2 and (g-i) HI3

percentage of HAGBs for the base metals and all the FZ welded samples. For AA6061-T6, the proportion of LAGBs was 56.15%, and for AA7075-T6, the proportion of LAGBs was 65.19%, respectively. For the HI1 joint, most of the MAs were greater than 15°, which corresponds to HAGBs, and the proportion of LAGBs was 41.82 %. However, for the HI2 joint, the proportion of LABs was 36.08 % and for HI3 joint, the proportion of LABs was 30.53 %. It can be concluded that the LAGBs in the BMs transformed into HAGBs in the FZ in the DS-TIG joints. In addition, a decrease in AGS of the grains leads to increase in LAGBs and decreased HAGBs (Ref 58), i.e., the proportion of LAGBs for HI1 joint is maximum and is minimum for the HI3 joint confirming that the grain transformations are more favorable for HI3 joint. The boundary MAs distribution is mostly linked to the different heating and cooling cycles that happen during welding, especially the peak

temperature that can be reached (Ref 54). The HI3 joint raises the FZ peak temperature, generating a high temperature gradient across grain boundaries. The higher diffusion at high peak temperatures may accelerate grain boundary migration and transformation. This may accelerate LAGBs to HAGBs. However, HI3 may cause excessive grain development and coarsening, which may harm mechanical qualities (Ref 15). Dislocations move slower in materials with higher HAGBs and fine grains when subjected to tensile tension. GBs experience an increase in dislocations. Higher resistance to external tensile stress deformation leads to increased joint strength and ductility (Ref 56).

Texture strengthening occurs when a material's mechanical properties improve as a result of a change in its texture (Ref 56). The texture variations were analyzed using the pole figures (PFs) and orientation distribution functions (ODFs) in
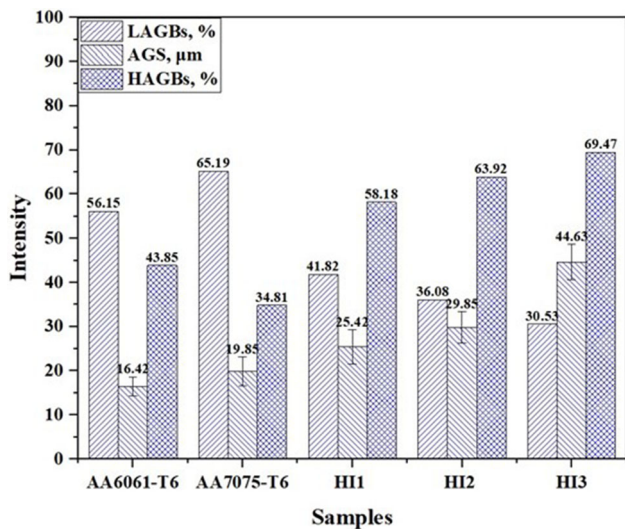
Fig. 9 Statistical results showing proportion of LAGBs, AGS and proportion of HAGBs in the base alloys and the DS-TIG joints

the center of the FZ regions of dissimilar weld joints (Fig. 11). Figure 10 depicts the basic standard textures for face centered cubic (FCC) materials, as described in the aforementioned literature (Ref 30, 59-61), positioned on the acquired PFs and ODFs for clarity. The several basic deformation textures for FCC material are demonstrated in Fig. 10(a), where they have been applied to PFs {001}, {101} and {111} (Fig. 10b). Figure 10(c) shows the ideal orientation of the texture components deformation, recrystallization, and plane strain on the ODF sections (see Fig. 10(d)) displayed in Euler space-Bunge notations at $\varphi_2 = 0°$, 45° and 65°. Figure 11(a), (b) and (c) represents the {001}, {101} and {111} PFs for the HI1, HI2 and HI3 joints, superimposed with the respective standard PFs. All the joints in FZ center exhibited strong dominance of A_1^*/ A_2^* and A/ $\overline{A}$ textures. The formation of the A_1^*/ A_2^* and A / $\overline{A}$ textures component (minor deformation texture components) indicate that this region (FZ) has undergone significant recrystallization at increased peak temperatures. The PFs also revealed small amount of major deformation texture components C and B / $\overline{B}$ in FZ that indicates that this region (FZ) has also undergone some deformations during welding process.

Figure 11(d), (e) and (f) represents the ODFs results of the samples HI1, HI2, and HI3 joints superimposed with the respective standard ODFs. The Brass, Copper, and S textures are related to plane strain texture components, the E, F, and H textures are originated from the deformation texture components, and Cube, Goss, and P are in a relation with recrystallization texture components (Ref 61). In ODF plot at $\varphi_2 = 0°$ and 45° section of Euler's space, the strong intensity recrystallization texture components P {011} <112> and Goss {110} <001> , plane strain texture component S {123} <634> with small amount of deformation texture component H {001} <110> are observed at $\varphi_2 = 65°$ in the FZ near weld center for all the three heat input samples. The presence of strong intensity recrystallization texture components Cube {001} <110> in the fusion region at $\varphi_2 = 0°$, and F {111} <112> at $\varphi_2 = 45°$ section are also observed in the midregion of FZ for all the three heat input samples. Therefore, it can be comprehended that all the heat input samples exhibited the significant strong intensity recrystallization textures namely

Cube {001} <100> , Goss {110} <001> , and P {011} <112> and some deformation texture components like H {001} <110> and F {111} <112> , which signifies the low amount of deformation also occurred in the FZ, which aligns with the current observations derived from Fig. 8. In addition, the highest orientation density value was approximately 7.05 in the HI3, 6.73 in the HI2, and 5.64 in the HI1 joints (Fig. 11d, e and f). The value of maximum orientation density is increased as the welding current and voltage is increased (Ref 31). The change in texture strengthening is associated with the different solidification behavior of the FZ formed at different heat inputs (Ref 62). The HI2 and HI3 joints feature stronger textures than the HI1 joint, which may reduce anisotropy and improve mechanical characteristics (Ref 60, 63).

3.4 Mechanical Properties

Table 4 summarizes mechanical characteristics of the base alloys and DS-TIG welded joints at various heat inputs. Welded joints have lower microhardness (MH), ultimate flexural strength (UFS), and ultimate tensile strength (UTS) relative to the base alloys. Figure 12(a) depicts the engineering stress–strain curves for DS-TIG joints subjected to varying heat inputs. The engineering stress–strain curves of AA6061-T6 and AA7075-T6 are also included for comparison. The UTS of HI1, HI2 and HI3, is 152, 182 and 141 MPa, respectively and the corresponding percentage elongation (PE) is 8.7, 14.4 and 6.2%, respectively. The HI1 joint had the lowest UTS and PE compared to the other joints, which may be due to the shallower penetration of the weld and the development of voids in the FZ. Lee (Ref 64) established a power–law relationship between AZ91 alloy tensile strength and vacancies. They found that voids considerably reduced both the tensile strength and ductility of the samples. So, even though the HI1 joint has the smallest average grain size (Fig. 8h), its poor tensile strength may be explained by the presence of macro-voids. The HI2 joint exhibits the largest UTS and PE compared with the other joints. Increased heat input resulted in relatively low cooling rates and prevented the molten pool from rapidly solidifying. Consequently, air has sufficient time to evacuate the molten pool, and the voids decrease (Fig. 6f). Additionally, in the HI2 joint, the secondary phases or precipitates like $MgZn_2$ and Al_2CuMg phases are segregated and distributed more uniformly in the FZ (Fig. 6g). Also, the average grain size (AGS) in the FZ (29.85 ± 13.68 μm) of HI2 joint is smaller than that in the FZ (44.63 ± 15.18 μm) of HI3 (Fig. 8e and h). However, the high heat input concentrations in the fusion region of the HI3 joint may result in the vaporization of Zn and Mg elements and a decrease in intermetallic $MgZn_2$ and Al_2CuMg precipitates (Fig. 7). The solid solution precipitate hardening of the HI3 joint is less affected by these components than the HI2 joint. These talks suggest that the HI2 joint is stronger than the HI3 joint. HI2 and HI3 joints are fractured in the HAZ of AA6061-T6, rather than in the FZ, as shown in Fig. 12(b).

Like tensile strength, all heat input samples had somewhat increased flexural strength (Fig. 13a). The top surface is compressed and the lower surface is tensioned during the root flexural test of the weld joint. The joint with the lowest UFS and flexural strain was HI1. Due to sound joint, HI2 joint exhibits highest UFS. HI3 joint has less UFS than HI2 joint owing to precipitate dissolution and grain coarsening. Flexural samples from DS-TIG joint root bending tests are shown in
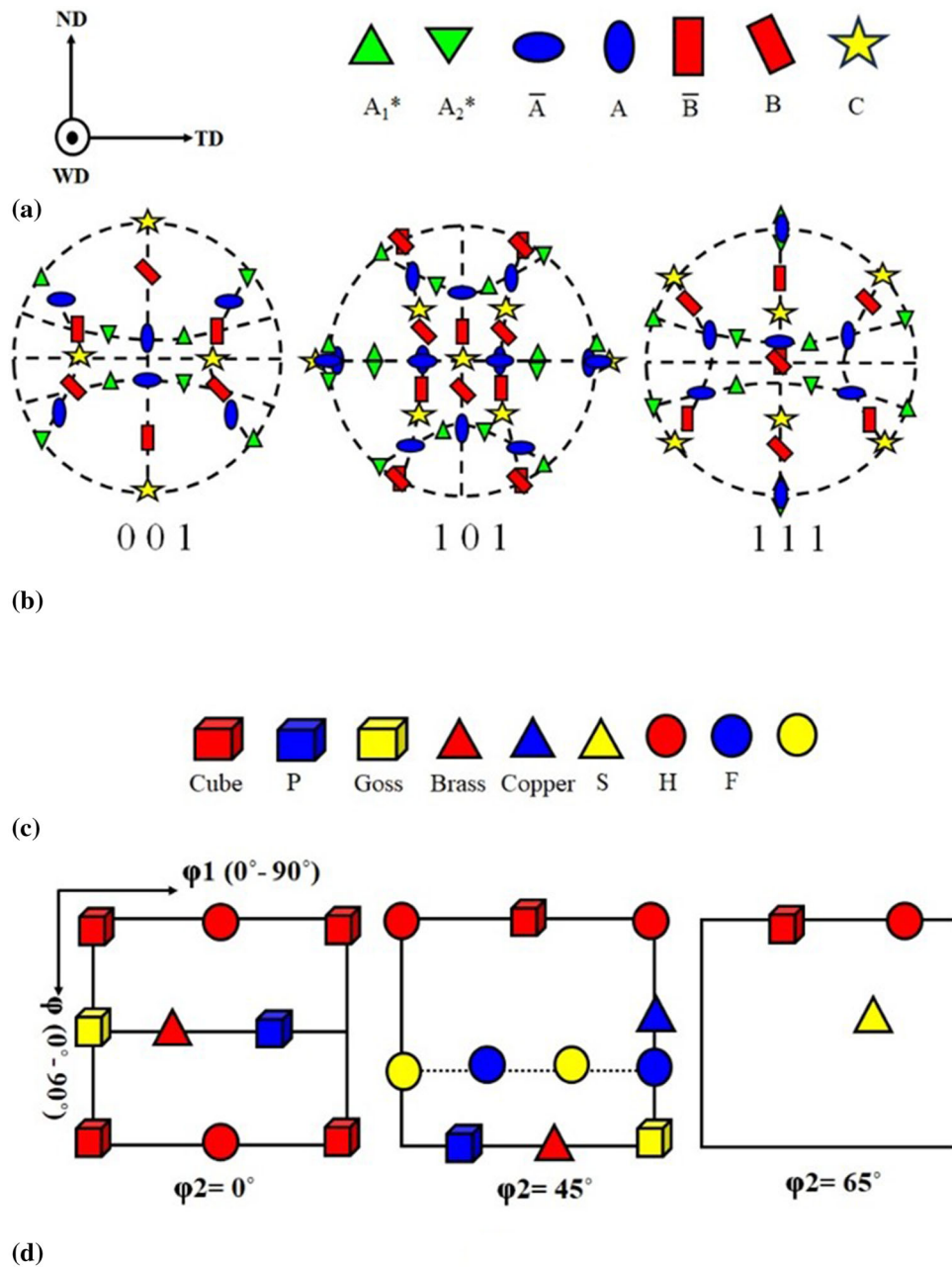
Fig. 10 Symbolic representation of (a) simple deformation texture components (b) ideally positioned over (001), (101) and (111) PFs (Ref 59, 60) and (c) texture components and (d) ideally positioned over ODF sections at φ = 0°, 45°, 65° (Ref 30, 61)

Fig. 13(b). HI1 joint seemed to rupture during bending testing, but HI2 and HI3 joints did not. HI2 had the greatest UFS without failures, suggesting appropriate joint parameters. The conclusions of this investigation corroborate earlier finding (Ref 22).

Figure 14(a), (b), (c) and (d) depicts SEM micrographs of the tensile fracture surfaces of samples HI1, HI2, and HI3, as well as EDS analysis of a selected region. Finer dimples result in increased joint strength and ductility; whereas, coarser dimples have the opposite effect (Ref 48). The fracture surface of the HI1 joint (Fig. 14a) is characterized by a large rough cleavage facet with some macro-voids. HI1 joint resulted in hydrogen entrapment inside the FZ attributed to its fast-cooling rate due to less time to combine and escape from the molten pool. These voids act as a stress concentrators and crack initiation sites, resulted brittle fracture mode (Ref 15). HI2 joint fracture surface (Fig. 15b) has homogenous, fine equiaxed dimples without porosities, suggesting ductile fracture mode. This shows that HI2 elongates more than other joints. HI3 joint fracture surface (Fig. 14c) has smooth and rough cleavage facets with coarser dimples, resulting in ductile and brittle fracture mode. EDS analysis (Fig. 14d) of selected red square region elucidates the presence of mainly 0.54% Mg, 2.04% Cu, 0.43% Zn, 2.74% Si, and 1.78% Fe along with aluminum. The reduced level of Mg and Zn confirms the dissolution of $MgZn_2$ and Al_2CuMg precipitates, which also validates the XRD findings. Therefore, HI2 results in lesser strength and percentage elongation than the HI3 joint.
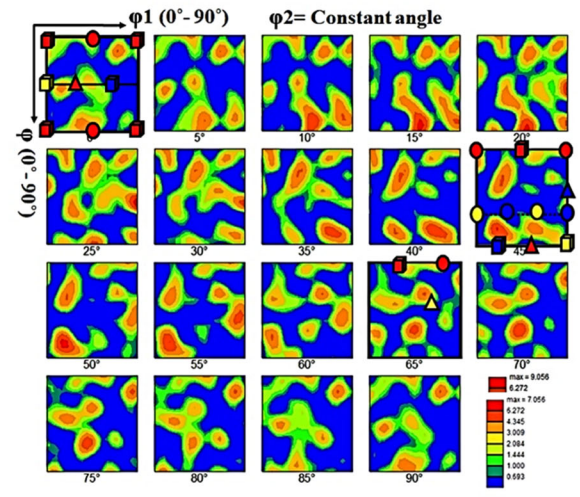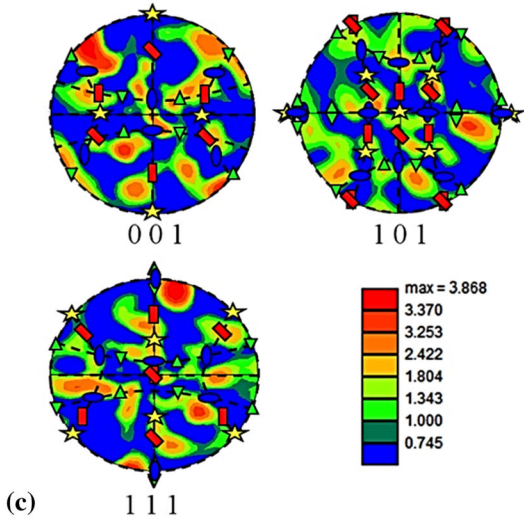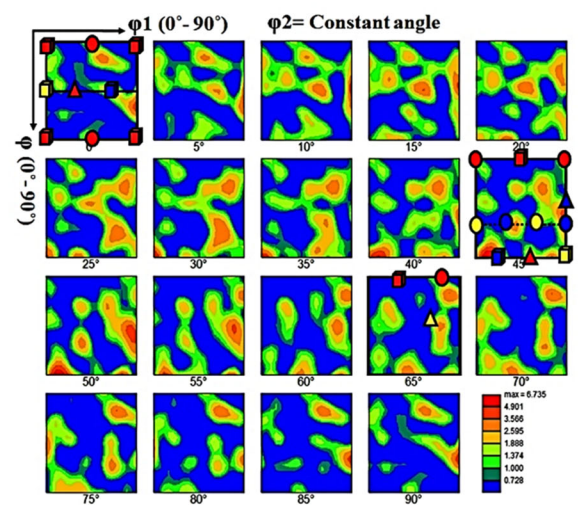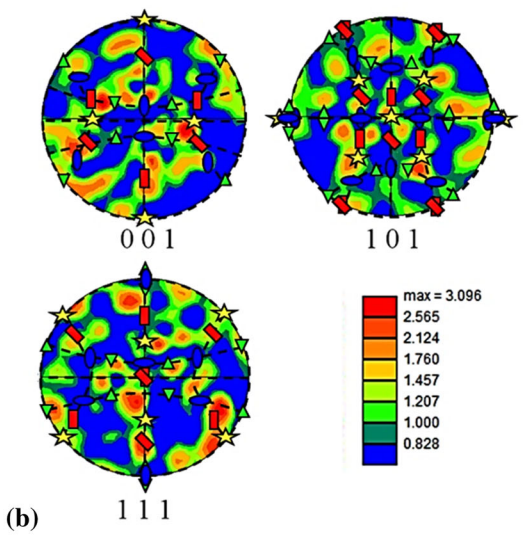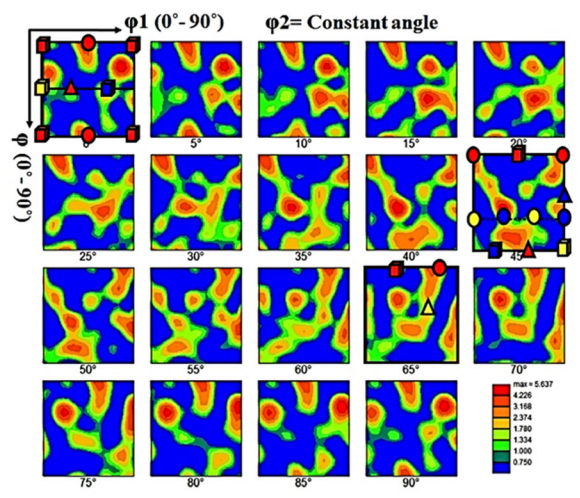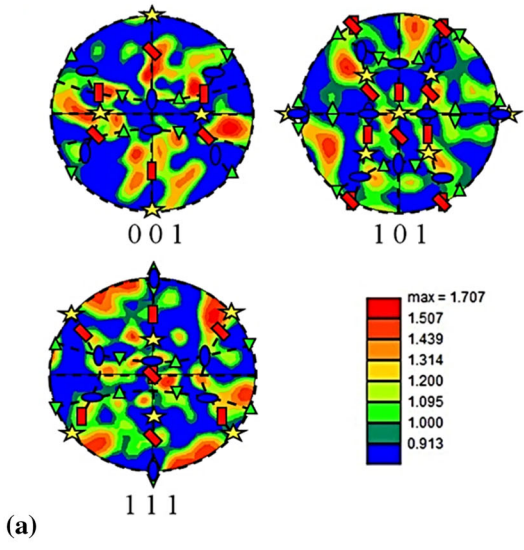
Fig. 11 PFs and ODFs (superimposed over respective standard PFs and ODFs) across the FZ of DS-TIG joints (a, d) HI1, (b, e) HI2 and (c, f) HI3

Table 4 Displays the mechanical characteristics of the base alloys and DS-TIG joints

Sample	Heat input, kJ/mm	Ultimate tensile strength, MPa	Percentage elongation, %	Ultimate flexural strength, MPa	Vickers microhardness, HV	Fracture location
AA6061-T6	…	281	21.8	401	114	…
AA7075-T6	…	488	12.3	610	147	…
HI1	0.73	130	5.8	142	81	FZ
HI2	1.69	182	14.4	202	75	AA6061 HAZ
HI3	2.27	168	11.2	186	58	AA6061 HAZ
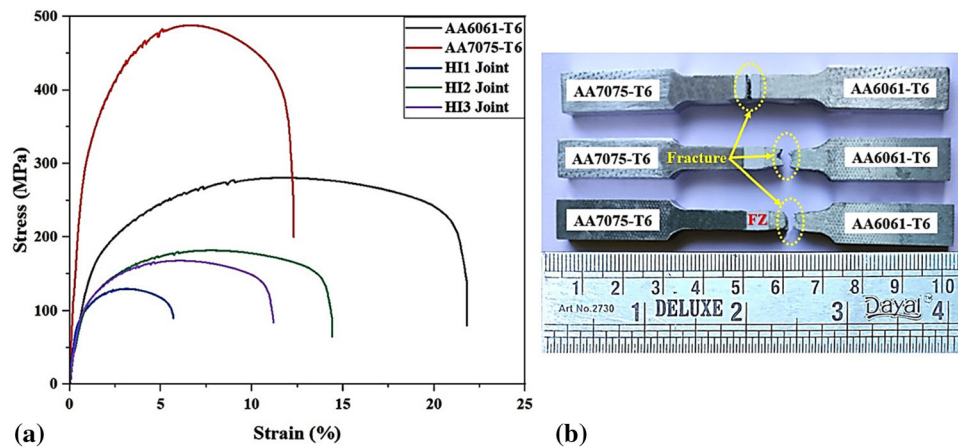
Fig. 12   (a) Tensile stress–strain curves of the DS-TIG joints and (b) the fracture location of joints at different heat inputs
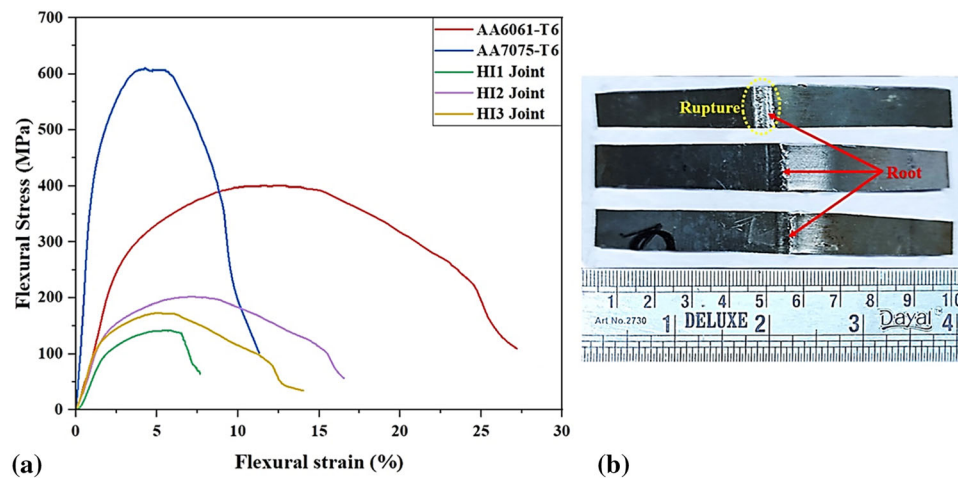

Fig. 13   (a) Flexural stress–strain curves of the DS-TIG joints and (b) the flexural samples after root bend test

Figure 15 depicts the consequence of heat input on the microhardness of the FZ and HAZs. A comparison of the hardness of FZ and HAZ in all the joints reveals that FZ is considerably harder than HAZ. This is due to the fact that FZ grains are considerably smaller than HAZ grains. It is observed that the tensile and flexural strengths are substantial material properties that are governed by the FZ's porosities. Hardness, on the other hand, is a local property that is mostly controlled by microstructural features like grain boundaries and grain size. The HI18, HI21, and HI24 joint average grain sizes are ∼ 25, 30, and 44 μm in FZ; while, it is ∼ 46, 62, and 81 μm in the HAZ of AA6061-T6 and ∼ 51, 67, and 92 μm in the HAZ of AA7075-T6, respectively. Because of this, FZ is able to achieve a greater hardness than HAZs. Moreover, the hardness values in AA6061 HAZ is slightly lesser than AA7075 HAZ, despite AA6061 HAZ has comparative finer grains. In actual, microhardness is also depending upon several other factors including temperature distribution, strain rate, and intermetallic precipitates proportion appear to have an influence on the microhardness of the weld metal (Ref 65).

The hardness results also show that as the heat input goes up, the hardness goes down. The HI1 joint is the hardest, even
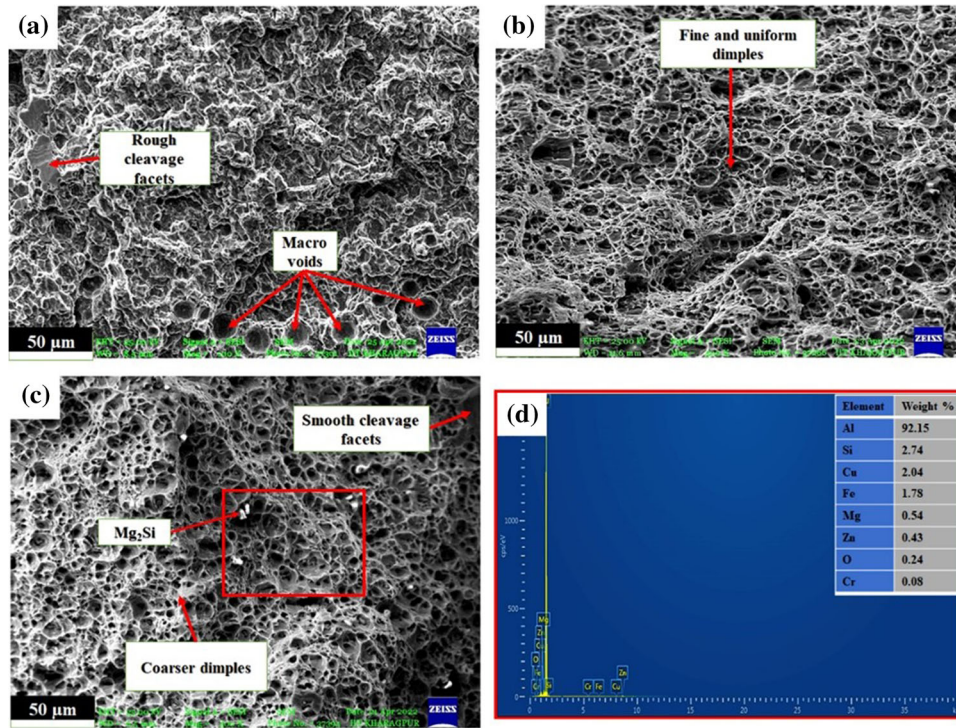
Fig. 14 SEM images of tensile fractured surfaces of the DS-TIG joints (a) HI1, (b) HI2, and HI3; (d) EDS analysis of selected red square region in (c) (Color figure online)
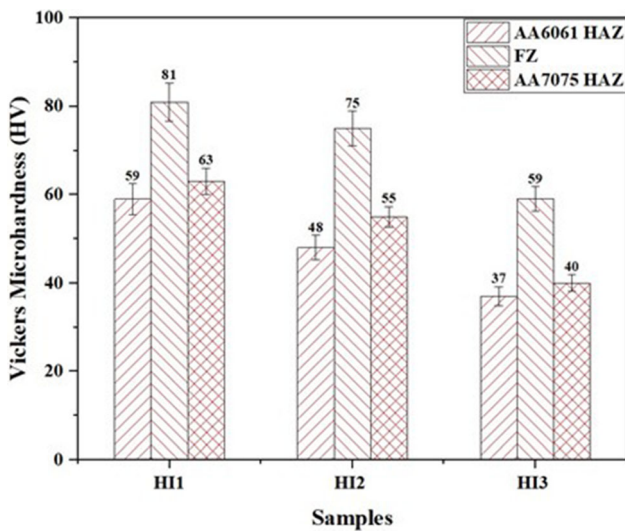
Fig. 15 Vickers microhardness of the FZ and HAZs of DS-TIG joints at various heat inputs

though its tensile and bending strengths are the lowest. According to Hall–Petch relationship $Hv = Hv_0 + kd^{\frac{-1}{2}}$, where d is grain size, Hv is the yield stress, Hv_0 and k are the constants associated with microhardness tests, and the strength of the hardness is inversely related to the size of the grains (Ref 66). Consequently, the HI1 with the AGS in FZ ($\sim$25 μm) has the greatest resilience. The HI3 joint, whose grain size in the FZ and HAZs is the greatest, demonstrates the lowest hardness. In addition, the transformation of LAGBs into HAGBs and the orientation density value are greatest in the HI3 joint (Fig. 8i and 11f), which provides high resistance to local deformation

during microhardness measurements, but HI3 exhibited the lowest hardness due to the loss of strengthening precipitates and grain coarsening. Therefore, it can be concluded that HI3 joint exhibited least microhardness due to the dissolution of precipitates and grain coarsening, despite having a maximum transformation of LAGBs into HAGBs and the higher orientation density value.

4. Conclusions

In this study, DS-TIG joints were made from AA6061-T6 and AA7075-T6 aluminum plates utilizing automated TIG welding and filler ER5356. The effects of heat inputs on joint microstructure and mechanical properties were studied. A detailed study of experimental results yielded the following primary findings:

1. The increase in heat input increased the dimensions of the weld bead, including the weld width, penetration depth, and PMZ breadth. However, the reinforcement initially increased but then decreased beyond a certain point with heat input. The best bead geometry was achieved with an HI2 (1.69 kJ/mm) joint at 145 A welding current, 20 V arc voltage, and 77 mm/min welding speed.

2. EBSD showed that LAGBs in base alloys transformed into high HAGBs in the FZ, with higher heat input. PFs revealed strong dominance of A_1^*/A_2^* and $A/\bar{A}$ textures with a small amount of C and $B/\bar{B}$ textures for all the heat input joints. ODFs also exhibited the recrystallization textures P {011} <112> and Goss {110} <001> , plane strain texture S {123} <634> with some deformation texture H {001} <110> at the FZ center.

3. The HI2 joint had the highest tensile strength of 182 MPa, elongation of 14.4%, and flexural strength of 202 MPa; while, the joint HI1 had the highest microhardness of 81 HV when compared to other joints. The increased proportion of HAGBs may have resulted in improved joint strengths, but excessive grain growth and coarsening resulted in decreased microhardness, despite greater LAGBs to HAGBs transformations.

4. The HI2 joint fracture surface displays fine dimples devoid of porosities, indicating ductile fracture mode. However, the fracture surface of the HI3 joint displayed both smooth and rough cleavage facets with coarser dimples, resulting in a combination of ductile and brittle fracture modes.

Acknowledgment

Conflict of interest

Authors in the present study did not report any conflict of interest.

References

1. R.I. Rodriguez, J.B. Jordon, P.G. Allison, T. Rushing and L. Garcia, Microstructure and Mechanical Properties of Dissimilar Friction Stir Welding of 6061-to-7050 Aluminum Alloys, *Mater. Des.*, 2015, **83**, p 60–65. https://doi.org/10.1016/j.matdes.2015.05.074

2. H. Mehdi and R.S. Mishra, Consequence of Reinforced SiC Particles on Microstructural and Mechanical Properties of AA6061 Surface Composites by Multi-pass FSP, *J. Adhes. Sci. Technol.Adhes. Sci. Technol.*, 2022, **36**, p 1279–1298. https://doi.org/10.1080/01694243.2021.1964846

3. R.S. Mishra, Z.Y. Ma and I. Charit, Friction Stir Processing: A Novel Technique for Fabrication of Surface Composite, *Mater. Sci. Eng. A*, 2003, **341**, p 307–310. https://doi.org/10.1016/S0921-5093(02)00199-5

4. M. Paidar, R. VairaVignesh, A. Moharrami, O.O. Ojo, A. Jafari and S. Sadreddini, Development and Characterization of Dissimilar Joint Between AA2024-T3 and AA6061-T6 by Modified Friction Stir Clinching Process, *Vacuum*, 2020, **176**, p 109298. https://doi.org/10.1016/j.vacuum.2020.109298

5. S. Memon, M. Paidar, O.O. Ojo, K. Cooke, B. Babaei and M. Masoumnezhad, The Role of Stirring Time on the Metallurgical and Mechanical Properties during Modified Friction Stir Clinching of AA6061-T6 and AA7075-T6 Sheets, *Results Phys.*, 2020 https://doi.org/10.1016/j.rinp.2020.103364

6. Z. Liu, K. Yang and D. Yan, Refill Friction Stir Spot Welding of Dissimilar 6061/7075 Aluminum Alloy, *High Temp. Mater. Processes (London)*, 2019, **38**, p 69–75. https://doi.org/10.1515/htmp-2017-0139

7. F. Ozturk, A. Sisman, S. Toros, S. Kilic and R.C. Picu, Influence of Aging Treatment on Mechanical Properties of 6061 Aluminum Alloy, *Mater. Des.*, 2010, **31**, p 972–975. https://doi.org/10.1016/j.matdes.2009.08.017

8. M. Temmar, M. Hadji and T. Sahraoui, Effect of Post-weld Aging Treatment on Mechanical Properties of Tungsten Inert Gas welded low Thickness 7075 Aluminium Alloy Joints, *Mater. Des.*, 2011, **32**, p 3532–3536. https://doi.org/10.1016/j.matdes.2011.02.011

9. M. Hakem, S. Lebaili, S. Mathieu, D. Miroud, A. Lebaili and B. Cheniti, Effect of Microstructure and Precipitation Phenomena on the Mechanical Behavior of AA6061-T6 Aluminum Alloy Weld, *Int. J. Adv. Manuf. Technol.*, 2019, **102**, p 2907–2918. https://doi.org/10.1007/s00170-019-03401-1

10. P. Bahemmat, M. Haghpanahi, M.K. Besharati, S. Ahsanizadeh and H. Rezaei, Study on Mechanical, Micro-, and Macrostructural Characteristics of Dissimilar Friction Stir Welding of AA6061-T6 and AA7075-T6, *Proc. Inst. Mech. Eng. B J. Eng. Manuf.*, 2010, **224**, p 1854–1865. https://doi.org/10.1243/09544054JEM1959

11. S. Jain, R.S. Mishra, H. Mehdi, R. Gupta and A.K. Dubey, Optimization of Processing Variables of Friction Stir Welded Dissimilar Composite Joints of AA6061 and AA7075 using Response Surface Methodology, *J. Adhes. Sci. Technol.Adhes. Sci. Technol.*, 2023 https://doi.org/10.1080/01694243.2023.2243682

12. B.C. Evik and M. Koç, The Effects of Welding Speed on the Microstructure and Mechanical Properties of Marine-grade Aluminium (AA5754) Alloy Joined using MIG Welding, *Metallic Materials/Kovové Materiály*, 2019, **57**, p 307–316.

13. M. Ishak, N.F. Mohd Noordin and L.H. Ahmad Shah, Feasibility Study on Joining Dissimilar Aluminum Alloys AA6061 and AA7075 by Tungsten Inert Gas (TIG), *J. Teknol.*, 2015 https://doi.org/10.11113/jt.v75.5177

14. S.S. Kumar and G. Godwin, An Enhancement of Properties on Al7075 and Al6061 Dissimilar Materials Welded by TIG Process, *Int. Res. J. Adv. Sci. Hub*, 2020, **2**, p 115–121. https://doi.org/10.47392/irjash.2020.47

15. M.S. Bin Reyaz and A.N. Sinha, Analysis of Mechanical Properties and Optimization of Tungsten Inert Gas Welding Parameters on Dissimilar AA6061-T6 and AA7075-T6 by a Response Surface Methodology-Based Desirability Function Approach, *Eng. Optim.Optim.*, 2023 https://doi.org/10.1080/0305215X.2023.2230133

16. G. İpekoğlu, S. Erim and G. Çam, Investigation into the Influence of Post-Weld Heat Treatment on the Friction Stir Welded AA6061 Al-Alloy Plates with Different Temper Conditions, *Metall. and Mater. Trans. A.*, 2014, **45**, p 864–877. https://doi.org/10.1007/s11661-013-2026-y

17. G. İpekoğlu and G. Çam, Effects of Initial Temper Condition and Postweld Heat Treatment on the Properties of Dissimilar Friction-Stir-Welded Joints between AA7075 and AA6061 Aluminum Alloys, *Metall. Mater. Trans. A*, 2014, **45**, p 3074–3087. https://doi.org/10.1007/s11661-014-2248-7

18. G. Çam, G. İpekoğlu and S.H. Tarık, Effects of use of Higher Strength Interlayer and External Cooling on Properties of Friction Stir Welded AA6061-T6 Joints, *Sci. Technol. Weld. Joining*, 2014, **19**, p 715–720. https://doi.org/10.1179/1362171814Y.0000000247

19. G. Çam and G. İpekoğlu, Recent Developments in Joining of Aluminum Alloys, *Int. J. Adv. Manuf. Technol.*, 2017, **91**, p 1851–1866. https://doi.org/10.1007/s00170-016-9861-0

20. N. Kashaev, V. Ventzke and G. Çam, Prospects of Laser Beam Welding and Friction Stir Welding Processes for Aluminum Airframe Structural Applications, *J. Manuf. Process.*, 2018, **36**, p 571–600. https://doi.org/10.1016/j.jmapro.2018.10.005

21. A. Heidarzadeh, S. Mironov, R. Kaibyshev, G. Çam, A. Simar, A. Gerlich et al., Friction Stir Welding/Processing of Metals and Alloys: A Comprehensive Review on Microstructural Evolution, *Prog. Mater. Sci. Mater. Sci.*, 2021, **117**, p 100752. https://doi.org/10.1016/j.pmatsci.2020.100752

22. A. Yürük, B. Çevik and N. Kahraman, Analysis of Mechanical and Microstructural Properties of Gas Metal Arc Welded Dissimilar Aluminum Alloys (AA5754/AA6013), *Mater. Chem. Phys.*, 2021 https://doi.org/10.1016/j.matchemphys.2021.125117

23. A.O. Al-Roubaiy, S.M. Nabat and A.D.L. Batako, Experimental and Theoretical Analysis of Friction Stir Welding of Al-Cu Joints, *Int. J. Adv. Manuf. Technol.*, 2014, **71**, p 1631–1642. https://doi.org/10.1007/s00170-013-5563-z

24. L. Kaba, M.E. Djeghlal, S. Ouallam and S. Kahla, Dissimilar Welding of Aluminum Alloys 2024 T3 and 7075 T6 by TIG Process with Double Tungsten Electrodes, *Int. J. Adv. Manuf. Technol.*, 2022, **118**, p 937–948. https://doi.org/10.1007/s00170-021-07888-5/Published

25. H. Mehdi and R.S. Mishra, Effect of Friction Stir Processing on Mechanical Properties and Wear Resistance of Tungsten Inert Gas Welded Joint of Dissimilar Aluminum Alloys, *J. Mater. Eng. Perform.*, 2021, **30**, p 1926–1937. https://doi.org/10.1007/s11665-021-05549-y

26. Tanmay and S.S. Panda, Characterisation of Cu–Al Alloy Lap Joint using TIG Welding, *CIRP J. Manuf. Sci. Technol.*, 2021, **35**, p 454–459. https://doi.org/10.1016/j.cirpj.2021.07.009

27. S. Jain and R.S. Mishra, A Review of the Effect of Process Parameters and Temperature Variation on FSWed Dissimilar Aluminium Alloys AA7075 and AA6061, *Emerging Trends Mech. Ind. Eng. Select Procee. ICETMIE*, 2023 https://doi.org/10.1007/978-981-19-6945-4_64

28. R. Crushan and V.P. Ashoka, Optimization of Dissimilar AA5052-H32 and AA5083-H111 Aluminium FSW Joints with Scandium Interfacial Layer, *Mater. Manuf. Processes*, 2023, **38**, p 1372–1384. https://doi.org/10.1080/10426914.2023.2165672

29. M. Raturi, A. Garg and A. Bhattacharya, Joint Strength and Failure Studies of Dissimilar AA6061-AA7075 Friction Stir Welds: Effects of Tool Pin, Process Parameters and Preheating, *Eng. Fail. Anal.*, 2019, **96**, p 570–588. https://doi.org/10.1016/j.engfailanal.2018.12.003

30. A. Garg, M. Raturi, A. Garg and A. Bhattacharya, Microstructure Evolution and Mechanical Properties of Double-sided Friction Stir Welding between AA6061-T6 and AA7075-T651, *CIRP J. Manuf. Sci. Technol.*, 2020, **31**, p 431–438. https://doi.org/10.1016/j.cirpj.2020.07.005

31. C. Chen, G. Sun, W. Du, Y. Li, C. Fan and H. Zhang, Influence of Heat Input on the Appearance, Microstructure and Microhardness of Pulsed Gas Metal Arc Welded Al Alloy Weldment, *J. Market. Res.*, 2022, **21**, p 121–130. https://doi.org/10.1016/j.jmrt.2022.09.028

32. H. Rojas, A. Molina, S. Valdez, B. Campillo, H. Martínez, A. Sedano et al., The Impact of Heat Input on the Microstructures, Fatigue Behaviors, and Stress Lives of TIG-welded 6061–T6 Alloy Joints, *Mater. Res. Express*, 2020, **7**, p 126512. https://doi.org/10.1088/2053-1591/abd136

33. M. Samiuddin, J. Li, M. Taimoor, M.N. Siddiqui, S.U. Siddiqui and J. Xiong, Investigation on the Process Parameters of TIG-welded Aluminum Alloy Through Mechanical and Microstructural Characterization, *Def. Technol.*, 2021, **17**, p 1234–1248. https://doi.org/10.1016/j.dt.2020.06.012

34. B. Çevik, Gas Tungsten Arc Welding of 7075 Aluminum Alloy: Microstructure Properties, Impact Strength, and Weld Defects, *Mater. Res. Express*, 2018, **5**, p 066540. https://doi.org/10.1088/2053-1591/aacbbc

35. M.S. Bin Reyaz and A.N. Sinha, An Experimental Investigation on Mechanical Characteristics and Wear Behaviour of TIG Welded Dissimilar Aluminum Alloys, *J. Adhes. Sci. Technol.Adhes Sci Technol*, 2023 https://doi.org/10.1080/01694243.2023.2251782

36. N. Çömez and H. Durmuş, Mechanical Properties and Corrosion Behavior of AA5754-AA6061 Dissimilar Aluminum Alloys Welded by Cold Metal Transfer, *J. Mater. Eng. Perform.*, 2019, **28**, p 3777–3784. https://doi.org/10.1007/s11665-019-04131-x

37. H. Ma, G. Qin, P. Geng, Z. Ao and Y. Chen, Effect of Intermetallic Compounds on the Mechanical Property and Corrosion Behaviour of Aluminium Alloy/steel Hybrid Fusion-brazed Welded Structure, *J. Manuf. Process.*, 2022, **75**, p 170–180. https://doi.org/10.1016/j.jmapro.2022.01.004

38. Z. Ye, J. Huang, W. Gao, Y. Zhang, Z. Cheng, S. Chen et al., Microstructure and Mechanical Properties of 5052 Aluminum Alloy/mild Steel butt Joint Achieved by MIG-TIG Double-sided Arc Welding-brazing, *Mater. Des.*, 2017, **123**, p 69–79. https://doi.org/10.1016/j.matdes.2017.03.039

39. Q. Qin, H. Zhao, J. Li, Y. Zhang, B. Zhang and X. Su, Microstructures and Mechanical Properties of TIG Welded Al-Mg2Si Alloy Joints, *J. Manuf. Process.*, 2020, **56**, p 941–949. https://doi.org/10.1016/j.jmapro.2020.05.058

40. Y. Guo, Y. Ma, X. Zhang, X. Qian and J. Li, Study on Residual Stress Distribution of 2024–T3 and 7075–T6 Aluminum Dissimilar Friction Stir Welded Joints, *Eng. Fail. Anal.*, 2020 https://doi.org/10.1016/j.engfailanal.2020.104911

41. B. Wang, B.B. Lei, J.X. Zhu, Q. Feng, L. Wang and D. Wu, EBSD Study on Microstructure and Texture of Friction Stir Welded AA5052-O and AA6061-T6 Dissimilar Joint, *Mater. Des.*, 2015, **87**, p 593–599. https://doi.org/10.1016/j.matdes.2015.08.060

42. H. Mehdi and R.S. Mishra, Microstructure and Mechanical Characterization of Tungsten Inert Gas-welded Joint of AA6061 and AA7075 by Friction Stir Processing, *Procee. Inst. Mech. Eng. Part L J. Mater. Design Appl.*, 2021, **235**, p 2531–2546. https://doi.org/10.1177/14644207211007882

43. R. Yamada, S. Ishizawa, G. Itoh, A. Kurumada, and M. Nakai. Effects of Environment on Fatigue Crack Growth Behavior of 2000 and 7000 Series Aluminum Alloys. Recent Advances in Structural Integrity Analysis - Proceedings of the International Congress (APCF/SIF-2014), Elsevier; 2014, pp 123–6. https://doi.org/10.1533/9780081002254.123

44. C. Rathinasuriyan and V.S.S. Kumar, Mechanical and Metallurgical Properties of GTAW, GMAW and FSW Lap Joints on AA6061-T6 Alloy, *Adv. Mater. Processing Technol.*, 2022, **8**, p 3231–3247. https://doi.org/10.1080/2374068X.2021.1946322

45. G.M.D. Cantin and J.A. Francis, Arc Power and Efficiency in Gas Tungsten Arc Welding of Aluminium, *Sci. Technol. Weld. Joining*, 2005, **10**, p 200–210. https://doi.org/10.1179/174329305X37033

46. N. Stenbacka, I. Choquet, and K. Hurtig. Review of arc efficiency values for gas tungsten arc welding. IIW Commission IV-XII-SG212, Intermediate Meeting, BAM, Berlin, Germany, 2012, pp 18–20

47. Y. Koli, N. Yuvaraj, S. Aravindan and Vipin, CMT Joining of AA6061-T6 and AA6082-T6 and Examining Mechanical Properties and Microstructural Characterization, *Trans. Indian Inst. Metals*, 2021, **74**, p 313–329. https://doi.org/10.1007/s12666-020-02134-0

48. D. Peng, J. Shen, Q. Tang, C.P. Wu and Y.B. Zhou, Effects of Aging Treatment and Heat Input on the Microstructures and Mechanical Properties of TIG-welded 6061–T6 Alloy Joints, *Int. J. Miner. Metall. Mater.*, 2013, **20**, p 259–265. https://doi.org/10.1007/s12613-013-0721-8

49. G. Song, Z. Wang, Z. Liu and L. Liu, Effect of Partial Rolling on the Microstructure and Mechanical Properties of Laser-TIG Hybrid Welded Joints of 7075–T6 Aluminum Alloy, *Int. J. Adv. Manuf. Technol.*, 2022, **121**, p 589–599. https://doi.org/10.1007/s00170-022-09287-w

50. N. Çömez and H. Durmus, Cold Metal Transfer Welding of AA6061 to AA7075: Mechanical Properties and Corrosion, *J. Eng. Mater. Technol. Trans. ASME*, 2019 https://doi.org/10.1115/1.4042863

51. I. Sevim, F. Hayat, Y. Kaya, N. Kahraman and S. Şahin, The Study of MIG Weldability of Heat-treated Aluminum Alloys, *Int. J. Adv. Manuf. Technol.*, 2013, **66**, p 1825–1834. https://doi.org/10.1007/s00170-012-4462-z

52. A.H. Eftekhar, S.M. Sadrossadat and M. Reihanian, Effect of Heat Input on Microstructure and Mechanical Properties of TIG-welded Semisolid Cast AXE622 Mg Alloy, *Mater CharactCharact.*, 2022 https://doi.org/10.1016/j.matchar.2021.111692

53. C. Liu, D.O. Northwood and S.D. Bhole, Tensile Fracture Behavior in CO_2 Laser Beam Welds of 7075–T6 Aluminum Alloy, *Mater. Des.Des.*, 2004, **25**, p 573–577. https://doi.org/10.1016/j.matdes.2004.02.017

54. S. Li, H. Dong, X. Wang, Z. Liu, Z. Tan, L. Shangguan et al., Effect of Repair Welding on Microstructure and Mechanical Properties of 7N01 Aluminum Alloy MIG Welded Joint, *J. Manuf. Process.*, 2020, **54**, p 80–88. https://doi.org/10.1016/j.jmapro.2020.03.009

55. H. Zhao, Q. Pan, Q. Qin, Y. Wu and X. Su, Effect of the Processing Parameters of Friction Stir Processing on the Microstructure and Mechanical Properties of 6063 Aluminum Alloy, *Mater. Sci. Eng. A*, 2019, **751**, p 70–79. https://doi.org/10.1016/j.msea.2019.02.064

56. M. Verma and P. Saha, Effect of Micro-grooves Featured Tool and their Depths on Dissimilar Micro-friction Stir Welding (μFSW) of Aluminum Alloys: A Study of Process Responses and Weld Characteristics, *Mater. CharactCharact*, 2023, **196**, p 112614. https://doi.org/10.1016/j.matchar.2022.112614

57. H. Zhao, M. Yu, Z. Jiang, L. Zhou and X. Song, Interfacial Microstructure and Mechanical Properties of Al/Ti Dissimilar Joints Fabricated via Friction Stir Welding, *J. Alloys Compd.*, 2019, **789**, p 139–149. https://doi.org/10.1016/j.jallcom.2019.03.043

58. N.S. Biradar and R. Raman, Grain Refinement in Al-Mg-Si Alloy TIG Welds using Transverse Mechanical Arc Oscillation, *J. Mater. Eng. Perform.*, 2012, **21**, p 2495–2502. https://doi.org/10.1007/s11665-012-0207-2

59. R.W. Fonda and J.F. Bingert, Texture Variations in an Aluminum Friction Stir Weld, *Scr. Mater.*, 2007, **57**, p 1052–1055. https://doi.org/10.1016/j.scriptamat.2007.06.068

60. M. Verma and P. Saha, Effect of Micro-grooves Featured Tool and their Depths on Dissimilar Micro-friction Stir Welding (μFSW) of Aluminum Alloys: A Study of Process Responses and Weld Characteristics, *Mater CharactCharact.*, 2023 https://doi.org/10.1016/j.matchar.2022.112614

61. M. Raturi and A. Bhattacharya, Microstructure and Texture Correlation of Secondary Heating Assisted Dissimilar Friction Stir Welds of Aluminum Alloys, *Mater. Sci. Eng. A*, 2021 https://doi.org/10.1016/j.msea.2021.141891

62. J. Li, H. Li, Y. Liang, P. Liu and L. Yang, The Microstructure and Mechanical Properties of Multi-strand, Composite Welding-wire Welded Joints of High Nitrogen Austenitic Stainless Steel, *Materials*, 2019 https://doi.org/10.3390/ma12182944

63. O.G. Rivera, P.G. Allison, L.N. Brewer, O.L. Rodriguez, J.B. Jordon, T. Liu et al., Influence of Texture and Grain Refinement on the Mechanical Behavior of AA2219 Fabricated by High Shear Solid State Material Deposition, *Mater. Sci. Eng. A*, 2018, **724**, p 547–558. https://doi.org/10.1016/j.msea.2018.03.088

64. C.D. Lee, Effect of Grain Size on the Tensile Properties of Magnesium Alloy, *Mater. Sci. Eng. A*, 2007, **459**, p 355–360. https://doi.org/10.1016/j.msea.2007.01.008

65. M. Tariq, I. Khan, G. Hussain and U. Farooq, Microstructure and Micro-Hardness Analysis of Friction Stir Welded Bi-layered Laminated Aluminum Sheets, *Int. J. Lightweight Mater. Manuf.*, 2019, **2**, p 123–130. https://doi.org/10.1016/j.ijlmm.2019.04.010

66. M.P. Alam and A.N. Sinha, Effect of Heat Assisting Backing Plate in Friction Stir Welding of High Strength Al-Li Alloy, *Energy Sour. Part A Recovery Util. Environ. Effects*, 2022, **44**, p 2851–2862. https://doi.org/10.1080/15567036.2019.1651793